Antisite disorder and Berry curvature driven anomalous Hall effect in the spin gapless semiconducting Mn_2CoAl Heusler compound

Nisha Shahi,[1] Ajit K. Jena,[2] Gaurav K. Shukla,[1] Vishal Kumar,[1] Shivani Rastogi,[1] K. K. Dubey,[1] Indu Rajput,[3] Sonali Baral,[3] Archana Lakhani,[3] Seung-Cheol Lee,[2] Satadeep Bhattacharjee,[2] and Sanjay Singh[1,*]

[1]*School of Materials Science and Technology, Indian Institute of Technology (Banaras Hindu University), Varanasi 221005, India*

[2]*Indo-Korea Science and Technology Center (IKST), Bangalore 560065, India*

[3]*UGC-DAE Consortium for Scientific Research, Indore 452001, India*

(Received 18 May 2022; revised 23 September 2022; accepted 28 November 2022; published 21 December 2022)

Spin gapless semiconductors exhibit a finite band gap for one spin channel and a closed gap for another spin channel, and they have emerged as a new state of magnetic materials with a great potential for spintronic applications. The first experimental evidence for spin gapless semiconducting behavior was observed in an inverse Heusler compound Mn_2CoAl. Here, we report a detailed investigation of the crystal structure and anomalous Hall effect in Mn_2CoAl using experimental and theoretical studies. The analysis of the high-resolution synchrotron x-ray diffraction data shows antisite disorder between Mn and Al atoms within the inverse Heusler structure. The temperature-dependent resistivity shows semiconducting behavior and follows Mooij's criteria for disordered metal. The scaling behavior of the anomalous Hall resistivity suggests that the anomalous Hall effect in Mn_2CoAl is primarily governed by an intrinsic mechanism due to the Berry curvature in momentum space. The experimental intrinsic anomalous Hall conductivity (AHC) is found to be ∼35 S/cm, which is considerably larger than the theoretically predicted value for ordered Mn_2CoAl. Our first-principles calculations conclude that the antisite disorder between Mn and Al atoms enhances the Berry curvature and hence the value of intrinsic AHC, which is in very good agreement with the experiment.

DOI: 10.1103/PhysRevB.106.245137

I. INTRODUCTION

The Hall effect is defined as the generation of a transverse voltage across a current-carrying conductor when an external magnetic field is applied perpendicular to the direction of the current flow [1–4]. An additional contribution in the transverse voltage was observed in materials with broken time-reversal symmetry (TRS), known as the anomalous Hall effect (AHE). It arises due to the mutual interaction of magnetization and spin-orbit coupling (SOC) [2,5]. The AHE, which was discovered more than a century ago, has attracted a vast amount of interest in recent years due to its role in understanding the fundamental physics [2,6–11] and the potential for applications in spintronics-based data storage devices and Hall sensors [12–19]. Theoretical studies suggest that the AHE could originate from both extrinsic and intrinsic mechanisms [6,20,21]. The extrinsic mechanism receives contributions from skew scattering and side jump mechanisms that are related to the asymmetric scattering and transverse shift of the propagation direction of spin-polarized charge carriers, respectively [22,23]. On the other hand, the intrinsic mechanism is related to the momentum space Berry curvature associated with the electronic band structure [20,24–26]. The momentum space Berry curvature acts as a fictitious magnetic field and introduces an anomalous velocity in addition to the group velocity of the electronic wave, perpendicular to the electric field direction, which creates intrinsic anomalous Hall conductivity (AHC) in the system [2,20,24].

The large AHC due to nonvanishing momentum space Berry curvature has been observed in various kinds of systems, such as $Nd_2Mo_2O_7$ [27], (In,Mn)As [28], (Ga,Mn)As [28], Mn_3Sn [29], Mn_3Ge [8], Fe_3Sn_2 [30], $Co_3Sn_2S_2$ [31], $CoNb_3S_6$ [32], and $SrIrO_3$ [33]. In addition to these materials, Heusler alloys have emerged as promising candidates for the realization of large Berry curvature originating from their peculiar band structure due to the integrated effect of crystal symmetry and SOC [34–38]. It has been observed that any small perturbation in the electronic band structure, such as, e.g., a local disorder, may affect the momentum space Berry curvature and therefore the intrinsic AHC in the system [39–43]. Recently, an enhanced intrinsic AHC was observed in Fe_2-based inverse Heusler compounds due to antisite disorder [44]. Also, a Berry curvature driven enhanced intrinsic AHC was observed in the Co_2FeAl Heusler compound, originating via antisite disorder between Fe and Al atoms [45].

The discovery of spin gapless semiconducting (SGS) behavior in the Mn_2CoAl Heusler compound puts this material forward as an important candidate for technological application in the field of spintronics [13,16,46,47]. Experimental studies on thin film as well as bulk systems of Mn_2CoAl reflect that most of the systems crystallize with compositional and/or antisite disorder, and the reported value of AHC is not in agreement with the theory [46,48–58]. A theoretical investigation considering antisite disorder suggests an enhancement in AHC, and it necessitates a detailed experimental and theoretical investigation to understand the origin of AHC in the Mn_2CoAl Heusler compound [59].

In the present manuscript, we investigate AHE in the Mn_2CoAl Heusler compound experimentally as well as the-

*ssingh.mst@itbhu.ac.in

oretically. The high-resolution synchrotron x-ray diffraction (SXRD) analysis exhibits 25% antisite disorder between Mn and Al atoms. The scaling behavior of anomalous Hall resistivity reveals the major contribution of the intrinsic mechanism in the observed AHE. Experimentally, we found a higher value of intrinsic AHC as compared to the value reported for an ordered Mn_2CoAl from theory [46,59]. Our theoretical calculations show that the antisite disorder between Mn and Al atoms enhances the Berry curvature and hence the value of intrinsic AHC, which is in good agreement with the experiment.

II. METHODS

The polycrystalline Mn_2CoAl Heusler compound is prepared using the arc-melting method [60–62]. The constituent elements (with purity higher than 99.9%) of the intermetallic system are melted in a water-cooled copper hearth under an argon atmosphere (purity better than 99.999%). The sample is remelted five times to ensure homogeneous mixing of the constituents. The chemical composition is verified using the energy-dispersive analysis of the x-ray technique. The average composition is found to be $Mn_{1.99}Co_{1.00}Al_{0.99}$, which corresponds to Mn_2CoAl. A small piece of the sample is powdered, and room-temperature synchrotron x-ray diffraction (SXRD) is performed in PETRA III DESY, Germany (wavelength ∼0.207 Å) for structural analysis. The direct current (DC) magnetization measurements are performed using a 9 T physical property measurement system (PPMS) of quantum design (QD). Transport measurements are carried out using an alternating current transport (ACT) option of 9 T PPMS of QD. Resistivity and magnetoresistance measurements are performed using the four-probe method, whereas the five-probe method is used for the Hall measurement. To remove the longitudinal resistivity contribution in the Hall data due to voltage probe misalignment, we have antisymmetrized the Hall resistivity data by using the formula $\rho_H = [\rho_H(+H) - \rho_H(-H)]/2$.

The spin-polarized Kohn-Sham Hamiltonian was solved within the framework of pseudopotentials (PPs) and plane waves as implemented in the QUANTUM ESPRESSO (QE) density-functional theory (DFT) package [63]. The exchange-correlation part of the above Hamiltonian is approximated by the generalized gradient approach [64] through ONCV Vanderbilt PPs [65]. The kinetic energy cutoff of 80 Ry is used to fix the number of plane waves. The same Gaussian smearing value (0.01 Ry) is used both for the self-consistent (SC) and non-self-consistent (NSC) calculations to carry out electronic integration over the Brillouin zone (BZ). A tight energy threshold (10^{-8} Ry) is considered for the SC energy calculations. We have used the WANNIER90 tool (implemented within QE) in order to compute the Wannier interpolated bands, Berry curvature, and AHC [63,66–68]. We note that spin-orbit coupling (SOC) is introduced in all the AHC-related calculations. Collinear spin-polarized calculations are also performed to compare some of our results with earlier reports, and they are mentioned at the appropriate places. The Monkhorst-Pack **k**-grid of $8 \times 8 \times 8$ of the BZ is considered in all the calculations, viz. SC, NSC, and WANNIER90. We found that the use of transition-metal d orbitals as the projections in the WANNIER90 calculations provide a good interpolation. A denser BZ **k**-grid of $75 \times 75 \times 75$ is taken to calculate the intrinsic AHC. Through the adaptive refinement technique, a further fine mesh of $5 \times 5 \times 5$ is added around the points wherever the mode of the Berry curvature [$|\Omega(\mathbf{k})|$] exceeds 100 bohr^2. The calculations are carried out using an experimental refined lattice constant of 5.858 Å.

III. RESULTS AND DISCUSSION

A. Structural characterization

To investigate the crystal structure of the Mn_2CoAl Heusler compound, the SXRD pattern was collected at room temperature. Mn_2YZ Heusler compounds generally exhibit XA-type (prototype Hg_2CuTi, space group $F\bar{4}3m$) crystal structure if the atomic number of Y is higher than the Mn-like Mn_2CoAl [69]. Therefore, in the primary step, we performed Rietveld refinement of SXRD data by assuming the XA-type crystal structure [Fig. 1(a)], using the FULLPROF software package [70]. In the refinement, the Mn atoms were considered at 4*a* (0,0,0) and 4*c* (0.25,0.25,0.25) Wyckoff positions, and they will be denoted as Mn_{4a} and Mn_{4c}, respectively. The Co and Al atoms were considered at 4*b* (0.50,0.50,0.50) and 4*d* (0.75,0.75,0.75) Wyckoff positions, respectively. It can be noticed from Fig. 1(a) that the observed and calculated peak profiles do not match with each other as the calculated intensity of the (111) superlattice peak is much larger than the observed intensity [depicted in the inset of Fig. 1(a)]. This mismatch between the calculated and observed intensities of Bragg peaks indicates that Mn_2CoAl does not crystallize in an ordered XA-type structure. In the next step, we tried the Rietveld refinement with the ordered $L2_1$ type ($Fm\bar{3}m$) crystal structure [Fig. 1(b)] [62,69], which also fails to account for the intensities of both the (111) and (200) superlattice reflections as depicted in Fig. 1(b) and its inset.

In the literature, it has been suggested that most of the inverse Heusler compounds crystallize with antisite disorder [44,62,69,71,72]. The antisite disorder in the Heusler compounds can generally be captured by analyzing the intensities of ordering-dependent (111) and (200) superlattice reflections [73]. For the Mn_2CoAl compound, the structure factor for (111), (200), and (220) reflections can be written as

$$F_{111} = 4\left[\left(f_{Mn_{4a}} - f_{Co}\right) - i\left(f_{Mn_{4c}} - f_{Al}\right)\right], \quad (1)$$

$$F_{200} = 4\left[\left(f_{Mn_{4a}} + f_{Co}\right) - \left(f_{Mn_{4c}} + f_{Al}\right)\right], \quad (2)$$

$$F_{220} = 4\left[\left(f_{Mn_{4a}} + f_{Co}\right) + \left(f_{Mn_{4c}} + f_{Al}\right)\right]. \quad (3)$$

Equation (1) suggests that the intensity of the (111) superlattice reflection is due to the difference between the atomic scattering factor (SF) of Mn_{4c} and Al atoms as the difference between the atomic SF of Mn_{4a} and Co atoms is negligible (since both are neighboring elements in the Periodic Table) and also the intensity of the (111) peak may change if the system has antisite disorder between the Mn_{4c} and Al atoms. From Eqs. (2) and (3), it is obvious that the intensities of (200) and (220) reflection will be unaffected by the antisite disorder between the Mn_{4c} and Al atoms. Hence, the mismatch between the observed and calculated intensities of the (111) peak in the Rietveld fitted SXRD pattern with XA-type crystal

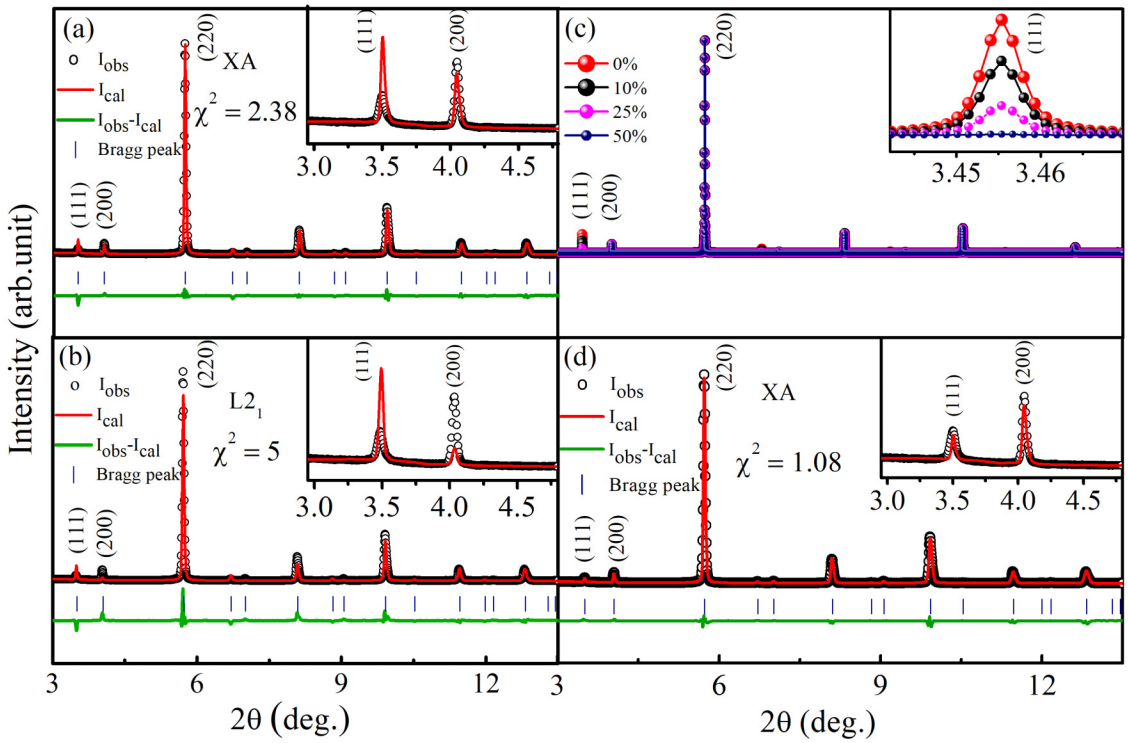

FIG. 1. (a) Rietveld profile fitting of the room-temperature (RT) synchrotron x-ray diffraction (SXRD) pattern of the Mn_2CoAl compound by considering the XA-type ordered structure. The observed profile (I_{obs}), the calculated profile (I_{cal}), and the difference between the observed and calculated profiles ($I_{obs} - I_{cal}$) are shown by a black circle, a red continuous line, and a green continuous line, respectively. The blue tick bars and the χ^2 value indicate the Bragg peak positions and the goodness of fit, respectively. (b) Rietveld profile fitting of the RT SXRD pattern of the Mn_2CoAl compound by considering the $L2_1$-type ordered structure. Insets in (a) and (b) show an enlarged view of the (111) and (200) peaks. (c) Simulated SXRD patterns considering the different percentage of antisite disorder between Mn_{4c} and Al atoms. The inset shows the variation in (111) peak intensity with the different percentage of antisite disorder. (d) Rietveld profile fitting of the RT SXRD pattern of Mn_2CoAl by considering 25% antisite disorder between Mn_{4c} and Al atoms. The inset shows an enlarged view around the (111) and (200) peaks.

structure suggests the presence of antisite disorder between Mn_{4c} and Al atoms.

Now, to find out the amount of antisite disorder, we simulated the SXRD pattern using VESTA software [74] by incorporating the different percentage of antisite disorder between Mn_{4c} and Al atoms within XA-type crystal structure as shown in Fig. 1(c). The inset of Fig. 1(c) represents an enlarged view of the change in intensity of (111) superlattice reflection with antisite disorder. We found that for 25% antisite disorder between Mn_{4c} and Al atoms, the intensity ratio of (111) superlattice reflection to the (220) fundamental reflection is in good agreement with the experiment. It is worthwhile to mention here that SXRD patterns simulated using other types of disorder such as disorder between Mn_{4a} and Mn_{4c}, between Mn_{4a} and Al, and between Co and Al do not provide an intensity ratio of Bragg reflections as observed in the experimental SXRD pattern. Therefore, based on the information obtained from Eqs. (1)–(3) and simulated SXRD patterns, in the final step we performed the Rietveld refinement considering 25% antisite disorder between the Mn_{4c} and Al atoms. A very good match between the observed and calculated peak profile was observed as depicted in Fig. 1(d). The inset of Fig. 1(d) shows an enlarged view of (111) and (200) peaks. The refined lattice parameter was obtained as ~5.858 Å, which is in good agreement with the literature [50].

B. Magnetization and resistivity measurements

The temperature variation of magnetization was measured in a temperature range of 2–400 K under a magnetic field of 1 T, as shown in Fig. 2(a). The magnetization decreases with increasing temperature, as expected for a ferrimagnetic system [75]. The observed behavior is similar to earlier reports [46,50]. Figure 2(b) presents the field-dependent magnetic isotherms [$M(H)$ curves] at 2 and 300 K. The negligible hysteresis is due to the soft magnetic nature of the Mn_2CoAl compound. The $M(H)$ curves show similar behavior in the entire temperature range of 2–300 K. To calculate the Curie temperature (T_c) of the present compound, the saturation magnetization (M_s) versus temperature [$M_s(T)$] data obtained from the $M(H)$ curves [black spheres in the inset of Fig. 2(b)] were fitted by the empirical law $M_s = M_0[1 - (T/T_c)^2]^{1/2}$ as shown by the red curve in the inset of Fig. 2(b) [56]. From this fitting, the T_c was found to be 720 K, which is in good agreement with the value reported in the literature [46,50,56]. The saturation magnetization of the present compound is found to be ~1.9 μB/f.u. at 2 K, which is in good agreement with the literature [46,56].

The monotonous decrease in the longitudinal resistivity (ρ_{xx}) with temperature [Fig. 2(c)] illustrates the semiconducting behavior of the present compound. A slight decrease in

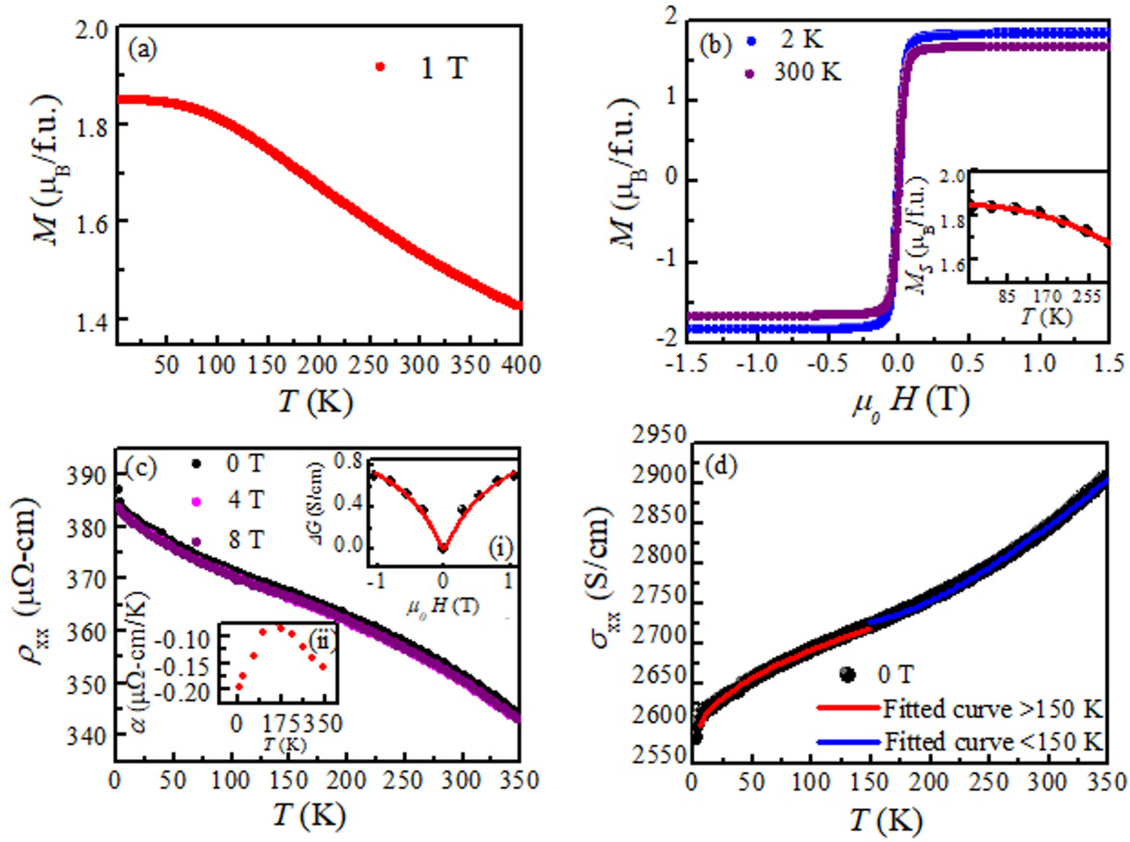

FIG. 2. (a) Temperature-dependent magnetization curve at 1 T magnetic field. (b) The isothermal field-dependent magnetization at different temperatures. The inset shows the fitting of saturation magnetization (M_s) vs temperature (T) with the empirical relation $M_s = M_0[1-(T/T_c)^2]^{1/2}$. The black dots and the red continuous line in the inset represent the M_s vs T data and the fitted curve, respectively. (c) Resistivity (ρ_{xx}) vs temperature (T) plot at different magnetic fields. Insets (i) and (ii) show the fitting of magnetoconductivity with field and the variation of temperature coefficient of resistivity (α) with temperature (T), respectively. (d) Fitting of conductivity (σ_{xx}) vs temperature (T) data in the temperature range below 150 K and in the higher temperature range above 150 K at zero field.

the value of ρ_{xx} with increasing magnetic field indicates the presence of small negative magnetoresistance in the system. The resistivity at 2 K (that corresponds to residual resistivity) is ∼387 μΩ cm, which is comparable to the reported one [50]. The residual resistivity ratio [ρ_{xx}(300 K)/ρ_{xx}(2 K)] was found to be ∼0.92, which is comparable to the value in the literature [46,50] and also suggests the presence of disorder in the Mn_2CoAl compound.

A theoretical calculation taking antisite disorder into account predicts a half-metallic character of the Mn_2CoAl Heusler compound in contrast to the SGS behavior [59,76]. It is interesting to note that the Mn_2CoAl compound shows semiconducting behavior [Fig. 2(c)] although a large (25%) antisite disorder is observed. It has been suggested in the literature that if the system has weak localization (WL), then inelastic scattering increases upon increasing the temperature, which may destroy the phase coherence, and hence the resistivity decreases with increasing temperature [77]. To check the possibility of WL in Mn_2CoAl, the magnetoconductivity (MC), i.e., a difference of conductivity between the finite magnetic field and zero field at room temperature, is fitted by an $H^{0.5}$ power law [shown in the inset (i) of Fig. 2(c)], which is well established for WL in three-dimensional (3D) systems [78–82], and it validates the presence of WL in bulk Mn_2CoAl. Further, Mooij established a correlation between the temperature coefficient of resistivity and residual resistivity for disordered metal, which describes how a disordered metal may exhibit semiconducting behavior if the residual resistivity exceeds 150 μΩ cm [83]. For Mn_2CoAl, a larger value of the residual resistivity (∼387 μΩ cm) is observed and follows Mooij's criteria.

The temperature coefficient of resistivity (α) for Mn_2CoAl changes from -0.9×10^{-9} to -1.9×10^{-9} Ω m/K in the temperature range of 2–350 K with a slope change around 150 K [shown in inset (ii) of Fig. 2(c)]. To understand the origin of the slope change in α, we analyzed the longitudinal conductivity ($\sigma_{xx} = 1/\rho_{xx}$) versus temperature data in the absence of magnetic field, and we found that σ_{xx} is proportional to $T^{1/2}$ below the temperature 150 K as shown in Fig. 2(d). This conductivity behavior follows the interaction theory at low-temperature according to Kaveh and Mott [84], which might be due to antisite disorder as supported by our SXRD analysis. Above 150 K, the conductivity variation with temperature follows the semiconducting-like character and is well approximated by the relation ($\sigma_{xx} = \sigma_0 + \sigma_a \exp^{E_g/K_BT}$) as shown in Fig. 2(d) [85]. The calculated band gap (E_g) from the best fitting was found to be ∼50 meV, which is of the same order as reported for the thin film of Mn_2CoAl [56]. Recently,

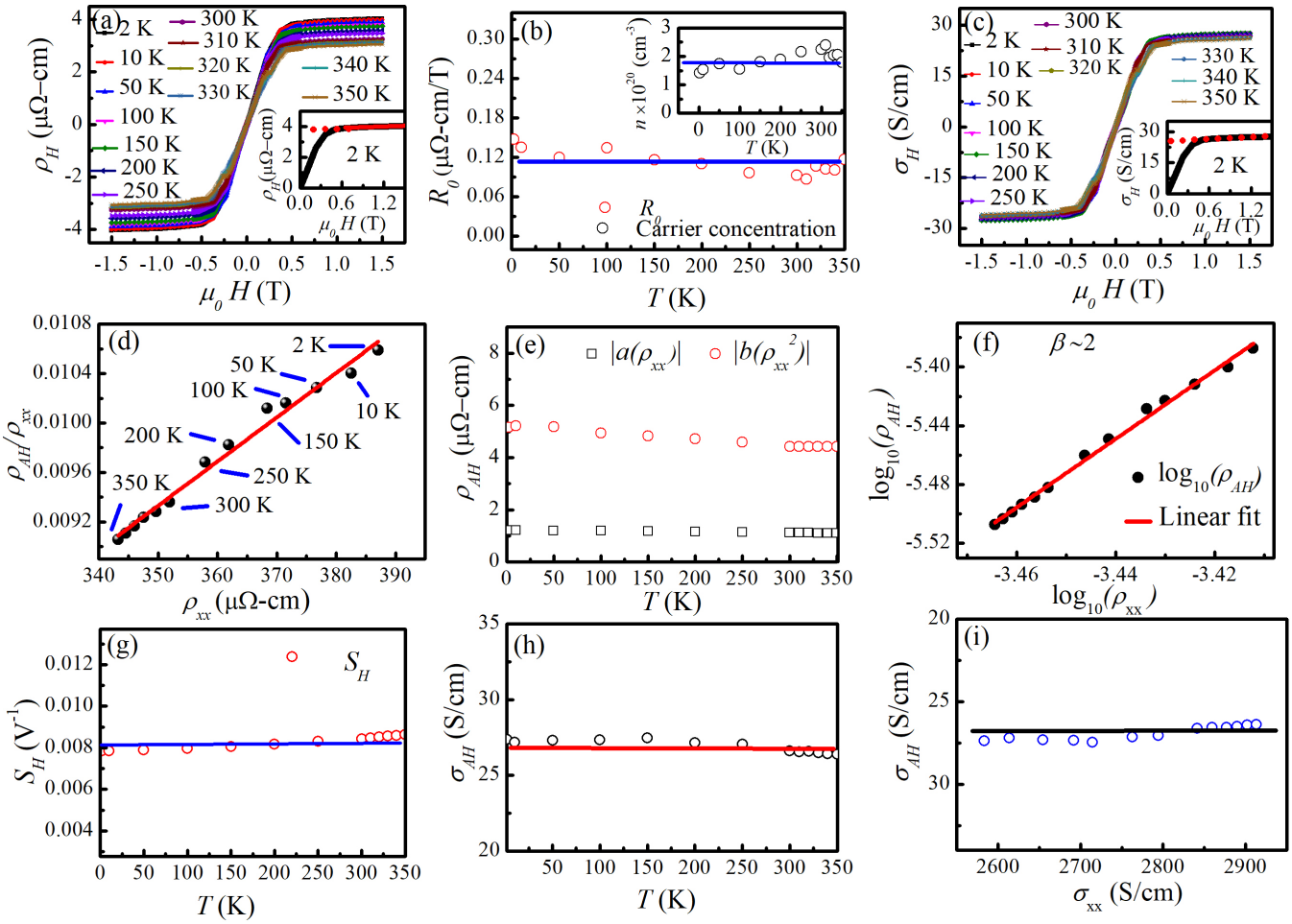

FIG. 3. (a) Field-dependent Hall resistivity curves at different temperatures. The inset shows the fitting of Hall data in the higher field region >0.6 T at 2 K. (b) Variation of the ordinary Hall coefficient with temperature. The inset shows carrier concentration vs temperature plot. (c) Field-dependent Hall conductivity curves at different temperatures. The inset indicates zero-field extrapolation of high-field Hall conductivity data at 2 K, shown by a red dotted line. (d) Fitting of the ratio of anomalous Hall resistivity and longitudinal resistivity (ρ_{AH}/ρ_{xx}) vs ρ_{xx} data. (e) Different contributions in ρ_{AH} with temperature are plotted on the same scale. (f) Linear fitting of $\log_{10}(\rho_{AH})$ vs $\log_{10}(\rho_{xx})$ data. (g) Variation of anomalous Hall scaling coefficient (S_H) with temperature. (h) Variation of AHC with temperature. (i) Variation of AHC with longitudinal conductivity.

an appreciable variation in the Seebeck effect around 150 K was observed in the polycrystal Mn_2CoAl [46]. This shows that our prepared compound is similar to the reported one, and the disorder present in the Mn_2CoAl compound is inherent and does not change with the sample preparation conditions.

C. Anomalous Hall measurement

Hall measurements were carried out in the temperature range of 2–350 K to investigate the anomalous transport behavior of the Mn_2CoAl compound. In general, the total Hall resistivity (ρ_H) consists of two parts, namely ordinary Hall and anomalous Hall, and it can be written as [1,86]

$$\rho_H = R_0 H + R_s M_s, \tag{4}$$

where R_0 and R_s are the ordinary and anomalous Hall coefficients, respectively. M_s corresponds to the saturation magnetization, and $R_s M_s$ represents the magnitude of anomalous Hall resistivity (ρ_{AH}). The field-dependent ρ_H data were recorded at different temperatures up to a magnetic field of 1.5 T, as shown in Fig. 3(a). The ρ_H increases steeply up to ∼0.6 T field, which is observed due to the AHE. At the higher field region (>0.6 T), ρ_H changes linearly and shows a positive slope with magnetic field, which is due to the ordinary Hall effect [37]. To separate out the ordinary and anomalous Hall contributions, we performed a fitting of the ρ_H versus H data by using Eq. (4) in the higher-field region (>0.6 T). The fitting of the ρ_H versus H data at 2 K, shown by the continuous red line in the inset of Fig. 3(a), provides the values of R_0 and $R_s M_s$ that correspond to the slope and intercept on the y axis of the fitted line. A similar analysis (i.e., fitting) is performed at various temperatures in the temperature range of 10–350 K, and Fig. 3(b) shows a temperature variation of R_0 obtained from the fitting. The positive value of R_0 in the whole temperature range (2–350 K) reveals that holes are the dominating charge carriers in the transport. The carrier concentration (n) determined by the expression $n = \frac{1}{eR_0}$ was found to be $\sim 1.5 \times 10^{20}$ and $\sim 2 \times 10^{20}$ cm^{-3} at 2 and 350 K, respectively. Thus, the value of n is nearly temperature-independent. The temperature variation of n for the temperature range 2–350 K

is depicted in the inset of Fig. 3(b), which is similar to that reported in the literature [46]. The Hall conductivity (σ_H) has been extracted by using the equation [35,41]

$$\sigma_{\mathrm{H}} = \frac{\rho_{\mathrm{H}}}{\rho_{\mathrm{H}}^2 + \rho_{\mathrm{xx}}^2}. \tag{5}$$

The field-dependent Hall conductivity at different temperatures is shown in Fig. 3(c). The value of AHC at 2 K is determined by zero-field extrapolation of the higher-field Hall conductivity curve as elucidated by the red dotted line in the inset of Fig. 3(c). The obtained value of AHC is 27 S/cm, which is comparable to the experimentally found value in the literature [46,50]. From the Berry curvature calculations, the AHC value was reported to be about 3 S/cm [46], which is an order of magnitude lower than the value obtained from the experiment (∼27 S/cm). To understand this discrepancy, it is necessary to address whether there is a contribution in the AHC from an extrinsic mechanism, such as skew scattering and side jumps, or from an intrinsic mechanism due to the momentum space Berry curvature associated with the electronic band structure.

To calculate the separate contributions of extrinsic and intrinsic mechanisms in the total AHC, the $\rho_{\mathrm{AH}}/\rho_{\mathrm{xx}}$ versus ρ_{xx} data [black dots in Fig. 3(d)] were fitted [red line in Fig. 3(d)] using the following relation [6,87,88]:

$$\rho_{\mathrm{AH}}/\rho_{\mathrm{xx}} = a + b\rho_{\mathrm{xx}}, \tag{6}$$

where the parameters a and b contain information about extrinsic skew scattering and the combined effect of an extrinsic side jump and an intrinsic contribution, respectively. We have used this scaling relation with the assumption that the ρ_{AH} will tend to zero as ρ_{xx} becomes very small. From the $\rho_{\mathrm{AH}}/\rho_{\mathrm{xx}}$ versus ρ_{xx} data fitting with the above equation, we obtained the value of $a \sim -0.003$ and $b \sim 35\ (\Omega\,\mathrm{cm})^{-1}$. The negative value of coefficient a indicates that the extrinsic skew scattering contribution is opposite to both the side jump and the intrinsic contribution due to momentum space Berry curvature. The value of parameter b contains the contributions in AHC due to both side jump and momentum space Berry curvature. By using the coefficients a and b, we calculated the skew scattering term ($a\rho_{\mathrm{xx}}$) and the intrinsic plus side jump term ($b{\rho_{\mathrm{xx}}}^2$) and plotted on the same scale as shown in Fig. 3(e). We can clearly see that the side jump together with the intrinsic contribution dominates over the skew scattering contribution in the overall AHE in the temperature range 2–350 K. We have observed that the ρ_{AH}, produced by using the above scaling relation, tends to zero as ρ_{xx} becomes very small.

The dominating mechanism in the AHE can be alternatively evaluated by the exponent β using the scaling relation $\rho_{\mathrm{AH}} \propto \rho_{\mathrm{xx}}^{\beta}$ [2,45]. If $\beta = 1$, the skew scattering mechanism will be dominant in the AHE, and if $\beta = 2$, the combination of the side jump and the intrinsic mechanism will largely contribute to the AHE. The exponent β determined by linear fitting of $\log_{10}(\rho_{\mathrm{AH}})$ versus $\log_{10}(\rho_{\mathrm{xx}})$ data [Fig. 3(f)] turns out to be 2, which also supports that the AHC is dominated by the side jump and the intrinsic mechanism [45]. It is not possible practically to separate out the side jump and intrinsic contributions because both contributions display a quadratic dependence on ρ_{xx} [2]. However, the AHC due to the side jump mechanism can be approximated using an expression $e^2/(ha)(E_{\mathrm{so}}/E_F)$, where E_{so} is the spin-orbit interaction energy and E_F is the Fermi energy [45,89]. The physical quantities e, h, and a are the electronic charge, Planck's constant, and the lattice parameter, respectively. Here, for Mn_2CoAl the σ_{xx} is $\sim 2.6\times10^3$ S/cm. Therefore, we may conclude that Mn_2CoAl is in the moderately dirty regime for which $E_{\mathrm{so}} \sim \hbar/\tau$, where $\hbar$ is the reduced Planck's constant, i.e., $h/2\pi$, and τ is the scattering time [2,90]. The calculated value of the ratio E_{so}/E_F for Mn_2CoAl is of the order of 10^{-3}, and hence in AHC the side jump contribution is negligible as compared to the Berry curvature induced intrinsic contribution. It has been suggested that the intrinsic AHC is nearly proportional to the magnetization, thus the scaling coefficient $S_H = \frac{\sigma_{\mathrm{AH}}}{M_s}$ should exhibit temperature-independent behavior if there is a dominant intrinsic contribution to the AHE [30,91]. Figure 3(g) depicts that the S_H for Mn_2CoAl is indeed independent of temperature, which indicates that the intrinsic contribution due to momentum space Berry curvature dominates over the extrinsic scattering contributions in the AHE [30,91]. The AHC shows a temperature-independent behavior [Fig. 3(h)] and does not vary with σ_{xx} as well [Fig. 3(i)]. This robust behavior of the AHC with the temperature and σ_{xx} further confirms that AHE in Mn_2CoAl originates mainly from the intrinsic mechanism, and is thus dominated by Berry curvature in momentum space [92].

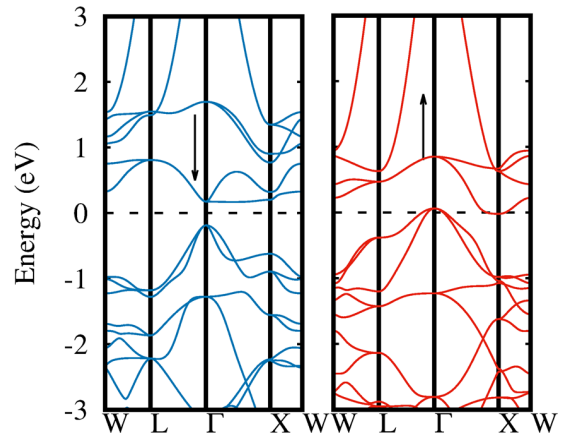

FIG. 4. Spin-polarized band structure of ordered Mn_2CoAl. Down and up arrows represent the spin-minority and -majority electrons, respectively.

D. First-principles calculations

In the literature, the value of AHC obtained from theory is much lower compared to the experiment [46]. Here, from the experiment, we found that the Mn_2CoAl has 25% disorder between Mn_{4c} and Al atoms. It is possible that this disorder may play an important role in the experimentally observed AHC, therefore we investigated the AHC in ordered and disordered Mn_2CoAl using theoretical calculations.

Before the discussion of AHC calculation, we first present our electronic structure results. The spin-polarized band structure of ordered Mn_2CoAl is shown in Fig. 4. The spin-minority channel has a finite gap, and the majority one has zero gap, which suggests the SGS feature of the

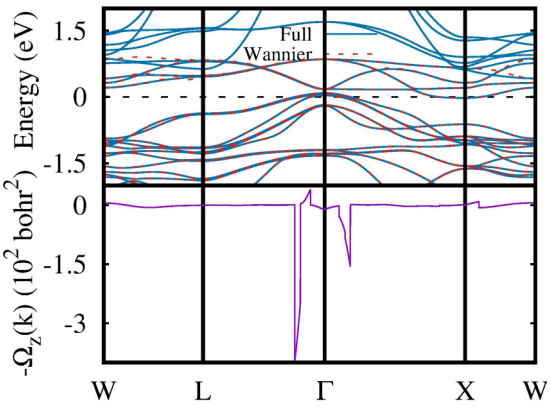

FIG. 5. Top: Full electronic band structure (blue continuous line) and Wannier interpolated band structure (red dashed line) of ordered Mn_2CoAl. The Fermi energy is set to 0 eV. Bottom: Distribution of the Berry curvature along the high-symmetry path in the Brillouin zone.

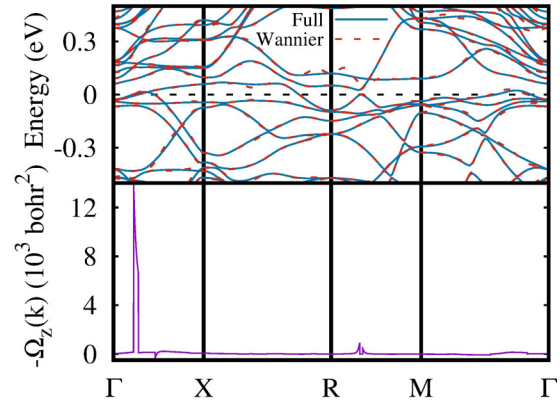

FIG. 6. Top: Full electronic band structure (blue continuous line) and Wannier interpolated band structure (red dashed line) of disordered Mn_2CoAl. The Fermi energy is set to 0 eV. Bottom: Distribution of the Berry curvature along the high-symmetry path in the Brillouin zone.

Mn_2CoAl compound. Spin gapless semiconductors offer intriguing transport properties because both the electrons and holes can be 100% spin-polarized, so that spin can be controlled via only a small applied external energy. The band structure for up and down spins shown in Fig. 4 matches very well with the literature [46]. Our calculated magnetic moment for the stoichiometric Mn_2CoAl is found to be $2\mu_{B/f.u.}$ with antiparallel coupling between Mn_{4a} and Mn_{4c} sites, which is also in agreement with the literature [46].

Now we will discuss the theoretical results on anomalous Hall transport obtained from WANNIER90. We compared the full DFT band structure of ordered Mn_2CoAl with the Wannier interpolated one in Fig. 5 (top), and we obtained a very good interpolation. The distribution of calculated Berry curvature along the high-symmetry path is shown in Fig. 5 (bottom). An efficient first-principles approach has been used in which the maximally localized Wannier functions are first constructed from the Bloch states, on a relatively coarse k-grid. Then the quantities of interest, e.g., Berry curvature, are interpolated onto a dense k-mesh in calculating the intrinsic AHC as a Brillouin zone summation of the Berry curvature over all occupied states [68,93],

$$\sigma_{xy}(\mathrm{AHC}) = \frac{e^2}{\hbar}\frac{1}{NV}\sum_{\mathbf{k}\in(\mathrm{BZ})}(-1)\Omega_{xy}(\mathbf{k})f(\mathbf{k}), \qquad (7)$$

where the indices x and y are the Cartesian coordinates. $f(\mathbf{k})$ is the Fermi distribution function, $\Omega_{xy}(\mathbf{k})$ denotes the Berry curvature for the wave vector $\mathbf{k}$, N is the number of electrons in the crystal, and V is the cell volume.

Our theoretical calculation gives intrinsic AHC value ~8.88 S/cm for the ordered Mn_2CoAl compound, which is slightly higher than the reported theoretical intrinsic AHC value of 3 S/cm [46]. This difference could be due to the two different approximations used to compute AHC. Thus, the theoretically calculated AHC for the ordered structure of the Mn_2CoAl compound is an order of magnitude smaller than the experimental value of intrinsic AHC ~35 S/cm. Therefore, to understand this difference, we performed the theoretical calculations by incorporating the amount of antisite disorder obtained from the SXRD experiment to compute the AHC. The magnetic moment obtained in this (disordered Mn_2CoAl) case was also found to be $\sim 2\mu_B$/f.u., which indicates that the antisite disorder does not affect the magnetization, and therefore electronic structure is most likely deciding the observed AHC in disordered Mn_2CoAl. In Fig. 6 (top), we have compared the full DFT band structure with the Wannier interpolated one for disordered structure. The distribution of calculated Berry curvature along the high-symmetry path is shown in Fig. 6 (bottom). Interestingly, the calculated intrinsic AHC in the disordered Mn_2CoAl increased to 26.30 S/cm, which is close to our experimentally obtained intrinsic AHC. In the present case, the disordered sample still possesses certain space group symmetry, which suggests that the disorder in the atomic positions will also be repeated in periodic units, and the theoretical calculation also considers the same. It is true that the value in the real samples could be slightly different from the theoretical results. The possible source of significantly less discrepancy in the value of experimental and theoretical intrinsic AHC for the disordered Mn_2CoAl could be the involved approximations in all steps of the theoretical calculations (starting from obtaining ground-state density to electronic and magnetic properties to Berry curvature computation to AHC). This suggests that the antisite disorder modifies the Berry curvature and hence enhances the intrinsic AHC in the Mn_2CoAl Heusler compound.

Recently, a comparative study of AHC between SGS Mn_2CoGa and half-metallic Co_2VGa compounds was performed, and it was reported that the Mn_2CoGa compound exhibits almost zero AHC, whereas half-metallic Co_2VGa (which has a similar magnetization and number of valence electrons to Mn_2CoGa) shows a larger AHC of about 140 S/cm [35]. The origin of this behavior was explained based on the electronic structure of these two compounds. SGS compounds are characterized by a finite gap in the minority-spin channel and a closed gap in the majority-spin channel, which results in a small number of majority-spin states around the Fermi level. In SGS compounds like Mn_2CoGa, the Berry curvature of majority-spin states is re-

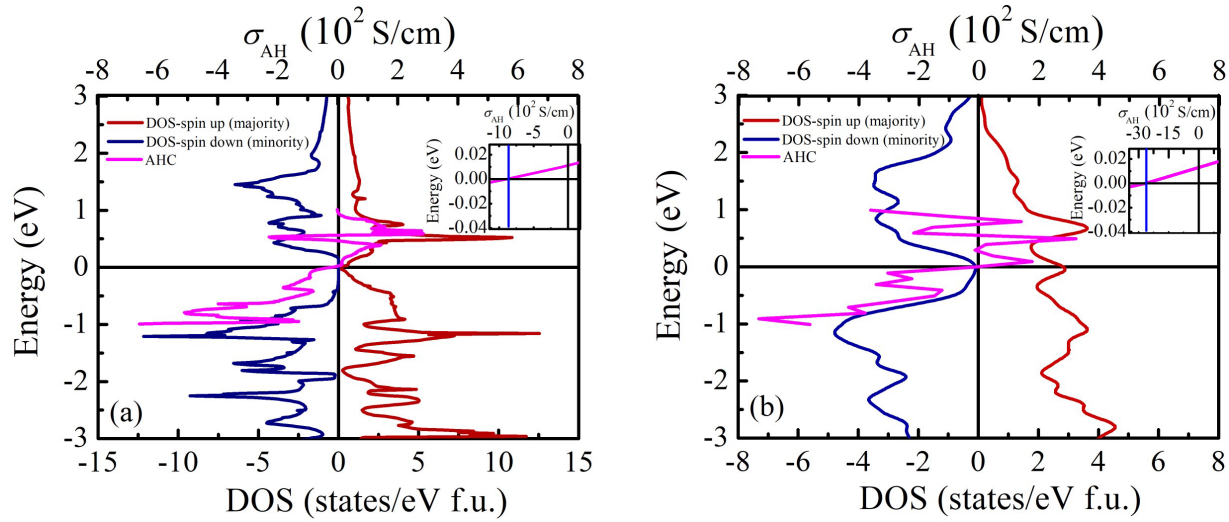

FIG. 7. (a) Density of states (DOS) and variation of intrinsic AHC of ordered Mn_2CoAl as a function of the Fermi energy. The Fermi energy is set to 0 eV. (b) DOS and variation of intrinsic AHC for the disordered Mn_2CoAl as a function of Fermi energy. The Fermi energy is set to 0 eV. Insets in (a) and (b) show an enlarged view of intrinsic AHC around the Fermi energy.

ported to cancel out by the minority-spin states resulting in a small/almost zero intrinsic AHC [35]. As compared to the SGS compounds, the half-metallic systems have a finite gap in the minority-spin channel and a large number of states in the majority-spin channel around the Fermi level [94]. In the half-metallic Co_2VGa compound, the large intrinsic AHC has been observed as compared to the Mn_2CoGa compound due to the uncompensated Berry curvature associated with a large number of majority-spin states [35]. Our study follows this behavior as the ordered Mn_2CoAl exhibits small intrinsic AHC due to its SGS nature [depicted in Fig. 7(a)], while upon introducing 25% disorder the system seems to be transformed from SGS to half-metallic due to the formation of new majority spin states around the Fermi level. This provides larger Berry curvature and leads to enhanced intrinsic AHC [depicted in Fig. 7(b)], which is in good agreement with the experiment. The insets of Figs. 7(a) and 7(b) show an enlarged view of the intrinsic AHC value around the Fermi level for ordered and disordered Mn_2CoAl compounds, respectively. Thus, our combined experimental and theoretical results show that atomic disorder enhances the intrinsic AHC due to the modification in the Berry curvature linked with the electronic structure in the Mn_2CoAl compound.

IV. CONCLUSION

To conclude, we have presented here the evidence of antisite disorder enhanced intrinsic AHC in the Mn_2CoAl Heusler compound by comprehensive analysis of the crystal structure and the anomalous Hall effect using experimental and theoretical tools. The high-resolution SXRD data reveal 25% antisite disorder between Mn_{4c} and Al atoms within the inverse Heusler structure. The temperature-dependent resistivity shows semiconducting behavior and follows Mooij's criteria for disordered metal. The scaling behavior suggests that the intrinsic mechanism dominates over the extrinsic mechanism in the AHE. The experimental intrinsic AHC is found to be larger than the theoretically reported value for the ordered Mn_2CoAl. The first-principles calculations conclude that the antisite disorder enhances the Berry curvature induced intrinsic AHC, which is in good agreement with the experimentally found intrinsic AHC.

ACKNOWLEDGMENTS

We gratefully acknowledge UGC-DAE CSR, Indore for experimental support. S.S. thanks Science and Engineering Research Board of India for financial support through the award of a Core Research Grant (Grant No. CRG/2021/003256). N.S. gratefully acknowledges the DST INSPIRE scheme for financial support. Parts of this research were carried out at PETRA III of DESY, a member of the Helmholtz Association. Financial support from the Department of Science and Technology, Government of India within the framework of India@DESY is gratefully acknowledged. We would like to express our gratitude towards the beamline scientist Dr. Martin Etter for his help in setting up the experiments.

[1] C. M. Hurd, *The Hall Effect in Metals and Alloys* (Plenum, New York, 1972).
[2] N. Nagaosa, J. Sinova, S. Onoda, A. H. MacDonald, and N. P. Ong, Rev. Mod. Phys. **82**, 1539 (2010).
[3] L. Šmejkal, A. H. MacDonald, J. Sinova, S. Nakatsuji, and T. Jungwirth, Nat. Rev. Mater. **7**, 482 (2022).
[4] S. Friedemann, M. Brando, W. J. Duncan, A. Neubauer, C. Pfleiderer, and F. M. Grosche, Phys. Rev. B **87**, 024410 (2013).
[5] T. Golod, A. Rydh, P. Svedlindh, and V. M. Krasnov, Phys. Rev. B **87**, 104407 (2013).
[6] Y. Tian, L. Ye, and X. Jin, Phys. Rev. Lett. **103**, 087206 (2009).

[7] R. Yu, W. Zhang, H.-J. Zhang, S.-C. Zhang, X. Dai, and Zhong Fang, Science **329**, 61 (2010).

[8] A. K. Nayak, J. E. Fischer, Y. Sun, B. Yan, J. Karel, A. C. Komarek, C. Shekhar, N. Kumar, W. Schnelle, J. Kübler, C. Felser, and S. S. P. Parkin, Sci. Adv. **2**, e1501870 (2016).

[9] C.-Z. Chang, J. Zhang, X. Feng, J. Shen, Z. Zhang, M. Guo, K. Li, Y. Ou, P. Wei, L.-L. Wang, Z.-Q. Ji, Y. Feng, S. Ji, X. Chen, J. Jia, X. Dai, Z. Fang, S.-C. Zhang, K. He, Y. Wang *et al.*, Science **340**, 167 (2013).

[10] S.-Y. Yang, Y. Wang, B. R. Ortiz, D. Liu, J. Gayles, E. Derunova, R. G.- Hernandez, L. Šmejkal, Y. Chen, S. S. P. Parkin, S. D. Wilson, E. S. Toberer, T. McQueen, and M. N. Ali, Sci. Adv. **6**, eabb6003 (2020).

[11] T. Taniguchi, J. Grollier, and M. D. Stiles, Phys. Rev. Appl. **3**, 044001 (2015).

[12] G. E. Bauer, E. Saitoh, and B. J. v. Wees, Nat. Mater. **11**, 391 (2012).

[13] S. K. Kim, G. S. D. Beach, K. J. Lee, T. Ono, T. Rasing, and H. Yang, Nat. Mater. **21**, 24 (2022).

[14] T. Jungwirth, X. Marti, P. Wadley, and J. Wunderlich, Nat. Nanotechnol. **11**, 231 (2016).

[15] L. Šmejkal, Y. Mokrousov, B. Yan, and A. H. MacDonald, Nat. Phys. **14**, 242 (2018).

[16] S. D. Bader and S. S. P. Parkin, Annu. Rev. Condens. Matter Phys. **1**, 71 (2010).

[17] R. J. Gambino and T. R. McGuire, IBM Tech. Disclosure Bull. **18**, 4 (1976).

[18] A. Gerber, J. Magn. Magn. Mater. **310**, 2749 (2007).

[19] J. Moritz, B. Rodmacq, S. Auffret, and B. Dieny, J. Phys. D **41**, 135001 (2008).

[20] R. Karplus and J. M. Luttinger, Phys. Rev. **95**, 1154 (1954).

[21] S. Onoda, N. Sugimoto, and N. Nagaosa, Phys. Rev. Lett. **97**, 126602 (2006).

[22] J. Smit and J. Volger, Physica (Amsterdam) **24**, 39 (1958).

[23] L. Berger, Phys. Rev. B **2**, 4559 (1970).

[24] M. V. Berry, Proc. R. Soc. Lond. A **392**, 45 (1984).

[25] X. Wang, D. Vanderbilt, J. R. Yates, and I. Souza, Phys. Rev. B **76**, 195109 (2007).

[26] J. M. Luttinger, Phys. Rev. **112**, 739 (1958).

[27] Y. Taguchi, Y. Oohara, H. Yoshizawa, N. Nagaosa, and Y. Tokura, Science **291**, 2573 (2001).

[28] T. Jungwirth, Q. Niu, and A. H. MacDonald, Phys. Rev. Lett. **88**, 207208 (2002).

[29] S. Nakatsuji, N. Kiyohara, and T. Higo, Nature (London) **527**, 212 (2015).

[30] Q. Wang, S. Sun, X. Zhang, F. Pang, and H. Lei, Phys. Rev. B **94**, 075135 (2016).

[31] Q. Wang, Y. Xu, and R. Lou, Nat. Commun. **9**, 3681 (2018).

[32] N. J. Ghimire, A. S. Botana, J. S. Jiang, J. Zhang, Y.-S. Chen, and J. F. Mitchell, Nat. Commun. **9**, 3280 (2018).

[33] M. W. Yoo, J. Tornos, A. Sander, L. F. Lin, N. Mohanta, A. Peralta, D. Sanchez-Manzano, F. Gallego, D. Haskel, J. W. Freel, D. J. Keavney, Y. Choi, J. Strempfer, X. Wang, M. Cabero, H. B. Vasili, M. Valvidares, G. Sanchez-Santolino, J. M. Gonzalez-Calbet, A. Rivera, S. G. E. Te Velthuis *et al.*, Nat. Commun. **12**, 3283 (2021).

[34] B. Ernst, R. Sahoo, Y. Sun, J. Nayak, L. Müchler, A. K. Nayak, N. Kumar, J. Gayles, A. Markou, G. H. Fecher, and C. Felser, Phys. Rev. B **100**, 054445 (2019).

[35] K. Manna, L. Muechler, T. H. Kao, R. Stinshoff, Y. Zhang, J. Gooth, N. Kumar, G. Kreiner, K. Koepernik, R. Car, J. Kübler, G. H. Fecher, C. Shekhar, Y. Sun, and C. Felser, Phys. Rev. X **8**, 041045 (2018).

[36] P. Li, J. Koo, W. Ning, J. Li, L. Miao, L. Min, Y. Zhu, Y. Wang, N. Alem, C. X. Liu, Z. Mao, and B. Yan, Nat. Commun. **11**, 3476 (2020).

[37] G. K. Shukla, J. Sau, N. Shahi, A. K. Singh, M. Kumar, and S. Singh, Phys. Rev. B **104**, 195108 (2021).

[38] J. Noky, Y. Zhang, J. Gooth, C. Felser, and Y. Sun, npj Comput. Mater. **6**, 77 (2020).

[39] J. Shen, Q. Yao, Q. Zeng, H. Sun, X. Xi, G. Wu, W. Wang, B. Shen, Q. Liu, and E. Liu, Phys. Rev. Lett. **125**, 086602 (2020).

[40] E. Vilanova Vidal, H. Schneider, and G. Jakob, Phys. Rev. B **83**, 174410 (2011).

[41] B. K. Hazra, M. M. Raja, R. Rawat, A. Lakhani, S. Kaul, and S. Srinath, J. Magn. Magn. Mater. **448**, 371 (2018).

[42] Z. Wang, Q. Liu, J. W. Luo, and A. Zunger, Mater. Horiz. **6**, 2124 (2019).

[43] S. Kastbjerg, N. Bindzus, M. Søndergaard, S. Johnsen, N. Lock, M. Christensen, M. Takata, M. A. Spackman, and B. B. Iversen, Adv. Funct. Mater. **23**, 5477 (2013).

[44] F. Mende, J. Noky, S. N. Guin, G. H. Fecher, K. Manna, P. Adler, W. Schnelle, Y. Sun, C. Fu, and C. Felser, Adv. Sci. **8**, 2100782 (2021).

[45] G. K. Shukla, A. K. Jena, N. Shahi, K. K. Dubey, I. Rajput, S. Baral, K. Yadav, K. Mukherjee, A. Lakhani, K. Carva, S.-C. Lee, S. Bhattacharjee, and S. Singh, Phys. Rev. B **105**, 035124 (2022).

[46] S. Ouardi, G. H. Fecher, C. Felser, and J. Kübler, Phys. Rev. Lett. **110**, 100401 (2013).

[47] X. L. Wang, Phys. Rev. Lett. **100**, 156404 (2008).

[48] K. Arima, F. Kuroda, S. Yamada, T. Fukushima, T. Oguchi, and K. Hamaya, Phys. Rev. B **97**, 054427 (2018).

[49] R. G. Buckley, T. Butler, C. Pot, N. M. Strickland, and S. Granville, Mater. Res. Express **6**, 106113 (2019).

[50] X. D. Xu, Z. X. Chen, Y. Sakuraba, A. Perumal, K. Ma-suda, L. S. R. Kumara, H. Tajiri, T. Nakatani, J. Wang, W. Zhou, Y. Miura, T. Ohkubo, and K. Hono, Acta Mater. **176**, 33 (2019).

[51] P. Chen, C. Gao, G. Chen, K. Mi, M. Liu, P. Zhang, and D. Xue, Appl. Phys. Lett. **113**, 122402 (2018).

[52] Y. Feng, C.-l. Tian, H.-k. Yuan, A.-l. Kuang, and H. Chen, J. Phys. D **48**, 445003 (2015).

[53] N. Y. Sun, Y. Q. Zhang, H. R. Fu, W. R. Che, C. Y. You, and R. Shan, AIP Adv. **6**, 015006 (2016).

[54] Y. Xin, H. Hao, Y. Ma, H. Luo, F. Meng, H. Liu, E. Liu, and G. Wu, Intermetallics **80**, 10 (2017).

[55] Y. J. Zhang, G. J. Li, E. K. Liu, J. L. Chen, W. H. Wang, and G. H. Wu, J. Appl. Phys. **113**, 123901 (2013).

[56] G. Z. Xu, Y. Du, X. M. Zhang, H. G. Zhang, E. K. Liu, W. H. Wang, and G. H. Wu, Appl. Phys. Lett. **104**, 242408 (2014).

[57] M. E. Jamer, B. A. Assaf, T. Devakul, and D. Heiman, Appl. Phys. Lett. **103**, 142403 (2013).

[58] K. Ueda, S. Hirose, and H. Asano, Appl. Phys. Lett. **110**, 202405 (2017).

[59] J. Kudrnovský, V. Drchal, and I. Turek, Phys. Rev. B **88**, 014422 (2013).

[60] B. Holt, J. Diaz, J. Huber, and C. A. Luengo, Revista Brasileira de Fisica **8**, 155 (1978).

[61] S. Singh, B. Dutta, S. W. D'Souza, M. G. Zavareh, P. Devi, A. S. Gibbs, T. Hickel, S. Chadov, C. Felser, and D. Pandey, Nat. Commun. **8**, 1006 (2017).
[62] S. Singh, R. Rawat, S. E. Muthu, S. W. D'Souza, E. Suard, A. Senyshyn, S. Banik, P. Rajput, S. Bhardwaj, A. M. Awasthi, R. Ranjan, S. Arumugam, D. L. Schlagel, T. A. Lograsso, A. Chakrabarti, and S. R. Barman, Phys. Rev. Lett. **109**, 246601 (2012).
[63] P. Giannozzi, S. Baroni, N. Bonini, M. Calandra, R. Car, C. Cavazzoni, D. Ceresoli, G. L. Chiarotti, M. Cococcioni, I. Dabo, A. D. Corso, S. de Gironcoli, S. Fabris, G. Fratesi, R. Gebauer, U. Gerstmann, C. Gougoussis, A. Kokalj, M. Lazzeri, L. Martin-Samos *et al.*, J. Phys.: Condens. Matter **21**, 395502 (2009).
[64] J. P. Perdew, K. Burke, and M. Ernzerhof, Phys. Rev. Lett. **77**, 3865 (1996).
[65] D. R. Hamann, Phys. Rev. B **88**, 085117 (2013).
[66] N. Marzari and D. Vanderbilt, Phys. Rev. B **56**, 12847 (1997).
[67] I. Souza, N. Marzari, and D. Vanderbilt, Phys. Rev. B **65**, 035109 (2001).
[68] G. Pizzi, V. Vitale, R. Arita, S. Blügel, F. Freimuth, G. Géranton, M. Gibertini, D. Gresch, C. Johnson, T. Koretsune, J. I.-Azpiroz, H. Lee, J.-M. Lihm, D. Marchand, A. Marrazzo, Y. Mokrousov, J. I. Mustafa, Y. Nohara, Y. Nomura, L. Paulatto, S. Poncé, T. Ponweiser *et al.*, J. Phys.: Condens. Matter **32**, 165902 (2020).
[69] T. Graf, C. Felser, and S. S. P. Parkin, Prog. Solid State Chem. **39**, 1 (2011).
[70] J. Rodríguez-Carvajal, FULLPROF, a Rietveld and pattern matching and analysis programs version 2016, Laboratoire Leon Brillouin, CEA-CNRS, France, http://www.ill.eu/sites/fullprof/.
[71] A. Nayak, M. Nicklas, S. Chadov, P. Khuntia, C. Shekhar, A. Kalache, M. Baenitz, Y. Skourski, V. K. Guduru, A. Puri, U. Zeitler, J. M. D. Coey, and C. Felser, Nat. Mater. **14**, 679 (2015).
[72] A. K. Nayak, M. Nicklas, S. Chadov, C. Shekhar, Y. Skourski, J. Winterlik, and C. Felser, Phys. Rev. Lett. **110**, 127204 (2013).
[73] G. D. Liu, X. F. Dai, H. Y. Liu, J. L. Chen, Y. X. Li, G. Xiao, and G. H. Wu, Phys. Rev. B **77**, 014424 (2008).
[74] K. Momma and F. Izumi, J. Appl. Crystallogr. **44**, 1272 (2011).
[75] L. N. Bezmaternykh, E. M. Kolesnikova, E. V. Eremin, S. N. Sofronova, N. V. Volkov, and M. S. Molokeev, J. Magn. Magn. Mater. **364**, 55 (2014).
[76] I. Galanakis, K. Özdoan, E. Şaşıoğlu, and S. Blügel, J. Appl. Phys. **115**, 093908 (2014).
[77] S. Dugdale, *The Electrical Properties of Disordered Metals* (Cambridge University Press, Cambridge, 1995).
[78] A. Kawabata, J. Phys. Soc. Jpn. **49**, 628 (1980)
[79] D. V. Baxter, R. Richter, M. L. Trudeau, R. W. Cochrane, and J. O. Strom-Olsen, J. Phys. France **50**, 1673 (1989).
[80] W. Chen, H.-Z. Lu, and O. Zilberberg, Phys. Rev. Lett. **122**, 196603 (2019).
[81] S. Malick, A. Ghosh, C. K. Barman, A. Alam, Z. Hossain, P. Mandal, and J. Nayak, Phys. Rev. B **105**, 165105 (2022).
[82] H. Afzal, S. Bera, A. K. Mishra, M. Krishnan, M. M. Patidar, R. Venkatesh, and V. Ganesan, J. Supercond. Nov. Magn. **33**, 1659 (2020).
[83] J. H. Mooij, Phys. Status Solidi A **17**, 521 (1973).
[84] M. Kaveh and N. F. Mott, J. Phys. C **15**, L707 (1982).
[85] K. Gofryk, D. Kaczorowski, T. Plackowski, A. Leithe-Jasper, and Y. Grin, Phys. Rev. B **72**, 094409 (2005).
[86] T. Kida, L. A. Fenner, A. A. Dee, I. Terasaki, M. Hagiwara, and A. S. Wills, J. Phys.: Condens. Matter **23**, 112205 (2011).
[87] P. He, L. Ma, Z. Shi, G. Y. Guo, J.-G. Zheng, Y. Xin, and S. M. Zhou, Phys. Rev. Lett. **109**, 066402 (2012).
[88] J. Kötzler and W. Gil, Phys. Rev. B **72**, 060412(R) (2005).
[89] P. Nozieres and C. Lewiner, J. Phys. **34**, 901 (1973).
[90] K. Kim, J. Seo, E. Lee, K.-T. Ko, B. S. Kim, B. G. Jang, J. M. Ok, J. Lee, Y. J. Jo, W. Kang, J. H. Shim, C. Kim, H. W. Yeom, B. I. Min, B.-J. Yang, and J. S. Kim, Nat. Mater. **17**, 794 (2018).
[91] C. Zeng, Y. Yao, Q. Niu, and H. H. Weitering, Phys. Rev. Lett. **96**, 037204 (2006).
[92] E. Liu, Y. Sun, N. Kumar, L. Muechler, A. Sun, L. Jiao, S. Y. Yang, D. Liu, A. Liang, Q. Xu, J. Kroder, V. Süß, H. Borrmann, C. Shekhar, Z. Wang, C. Xi, W. Wang, W. Schnelle, S. Wirth, Y. Chen, S. T. B. Goennenwein *et al.*, Nat. Phys. **14**, 1125 (2018).
[93] J. Kübler and C. Felser, Phys. Rev. B **85**, 012405 (2012).
[94] D. Rani, L. Bainsla, A. Alam, and K. G. Suresh, J. Appl. Phys. **128**, 220902 (2020).